Research Square

Preprints are preliminary reports that have not undergone peer review. They should not be considered conclusive, used to inform clinical practice, or referenced by the media as validated information.

The thermochemical non-equilibrium scale effects of the high enthalpy nozzle

Junmou Shen (shenjunmou@163.com)
China Academy of Aerospace and Aerodynamics https://orcid.org/0000-0003-1242-8007
Hongbo Lu
China Academy of Aerospace and Aerodynamics
Ruiqu Li
China Academy of Aerospace and Aerodynamics
Xing Chen
China Academy of Aerospace and Aerodynamics
Handong Ma
China Academy of Aerospace and Aerodynamics

Research

Keywords: high enthalpy nozzle, hypervelocity free flow, thermochemical non-equilibrium flow, scale effects

Posted Date: July 7th, 2020

DOI: https://doi.org/10.21203/rs.3.rs-20739/v3

License: This work is licensed under a Creative Commons Attribution 4.0 International License.
Read Full License

Version of Record: A version of this preprint was published on August 10th, 2020. See the published version at https://doi.org/10.1186/s42774-020-00044-9.

Abstract

The high enthalpy nozzle converts the high enthalpy stagnation gas into the hypervelocity free flow. The flow region of the high enthalpy nozzle consists of three parts: an equilibrium region upstream of the throat, a non-equilibrium region near the throat, and a frozen region downstream of the throat. Here we propose to consider the thermochemical non-equilibrium scale effects in the high enthalpy nozzle. With numerical solving axisymmetric compressible Navier-Stokes equations coupling with Park's two-temperature model, the fully non-equilibrium solution is employed throughout the entire nozzle. Calculations are performed at different stagnation conditions with the different absolute scales and expansion ratio. The results of this study contain twofold. Firstly, as the absolute scale and expansion ratio increase, the freezing position is delayed, and the flow approaches equilibrium. Secondly, the vibrational temperature and Mach number decrease with the increase in the nozzle scale and expansion ratio，while the speed of sound, static pressure, and translational temperature increase as the nozzle scale and expansion ratio increase.

Introduction

An important characteristic of non-equilibrium is its scale effects[1]. A large deal of research focuses on the scale effects of the test model and the actual aircraft[1,2], but little research has been published on the scale effects of the high enthalpy nozzle[3], especially the thermochemical non-equilibrium scale effects on the high enthalpy tunnel simulation ability. There are many high enthalpy tunnels in the world, such as TCM2[4], HEG[5],T4[6], T5[6], HIEST[6], JF-10[7], LENS I[8], and FD-21[9]. Due to the complexity and difficulty of the hypervelocity simulation, a great number of national and international space and hypersonic flight projects have been carried out extensively, such as integrated scramjet configuration[10], complex hypersonic flight configuration[10], and hypersonic boundary layer transition[11]. The experimental data obtained from the same test model are some differences under the similar stagnation gas and boundary condition. Except for the factors of the flowfield quality of the high enthalpy tunnel, the diameters of the high enthalpy nozzles range from 0.4m to 2.0m.

The flow regimes in hypervelocity nozzle flow exhibit two types of scale effects[1,12]. One of these scale effects, caused by viscosity, is confined to the boundary layer near the nozzle wall and can be avoided when simulating on the ground. The other is the thermochemical non-equilibrium scale effects, which must be taken seriously as it affects the entire flow field including the core flow region; it is this scale effects that is the focus of this article. The high enthalpy convergent-divergent nozzle flow is a complex process, especially nozzle divergence, because of the large range of Reynolds number scale and the high-temperature effects[13]. As evidenced in previous studies, there are three distinct flow regions: an upstream near the equilibrium region, a non-equilibrium region near the throat, and frozen flow not far downstream of the throat[12]. When the flow is nearly frozen, there are no longer the non-equilibrium scale effects in the expansion zone. The flow parameters and chemical species depend on the dissociation of non-equilibrium before the freezing point.

This paper investigates the thermochemical non-equilibrium scale effects of the high enthalpy nozzle by the numerical method. To verify the reliability of the numerical method, the HEG and TCM2 nozzles are used to calibrate. Because they have undergone many tests and numerical validation. Based on the HEG nozzle, the flow field of the nozzles scale when halved normal scale, normal scale, doubled normal scale and quintupled normal scale are numerically calculated. This paper also calculates the halved normal scale and normal scale of the FD-21 nozzle and the different expansion ratio based on the FD-21 nozzle. FD-21 was built in China Academy of Aerospace Aerodynamics in 2016 and is the largest-scale free-piston shock tunnel in the world[14,15].

At present, the three models of 5-species(O_2, N_2, NO, O, N), 7-species(O_2, N_2, NO, O, N, NO^+, e^-), and 11-species(O_2, N_2, NO, O, N, NO^+, O^+, N^+, O_2^+, N_2^+, e^-) are used to calculate the high enthalpy flow field[1,6,8,11]. The calculation results show that the flow field pressure, temperature, velocity and distribution of major chemical species are broadly coincident[4,5,11]. The ions of 7-species and 11-species, more than 5-species belong to the microspecies, and the chemical energy contained in them is negligible relative to the total gas flow, so they do not affect the main flow and the thermochemical parameters[12]. When it comes to questions such as flow field ionization and radiation characteristics, it is necessary to use the 7-species or 11-species models.

The 5-species and 7-species are used to calculate the high enthalpy flowfield in this paper. The axisymmetric compressible Navier-Stokes equations with Park's two-temperature model[16] are solved with a multi-block finite volume method. The results show that the freezing point moves downstream as the nozzle scale and ER increase. The flowfield characteristics, such as static temperature, Mach number, and species mass concentration distribution, are related to its absolute position, namely the nozzle scale. The larger nozzle scale and ER can effectively suppress thermochemical non-equilibrium flow, which are more suitable for simulating the flight environment.

Numerical Methods

Due to technological limitations, the Numerical Methods section is only available as a download in the supplementary files.

Verification Of Calculation Procedure

Due to technological limitations, the Verification of Calculation Procedure section is only available as a download in the supplementary files.

Discussion Of Results

4.1 Freezing point position

Numerical results of the different scale nozzles are now presented. The centerline evolution of the vibrational temperature T_V and translational temperature T are plotted in Fig.5. Not far downstream of the nozzle throat, the larger-scale nozzle has a slightly higher translational temperature. The vibrational temperature modifies the translational temperature, as deduced from the kinetic energy in Eq. (10). Compared with the translational temperature, the vibrational temperature is more affected by the absolute scale. The larger the scale, the further away from the throat the freezing point, and the lower the vibrational temperature. The vibrational temperature of 0.5NS, NS, 2NS, 5NS is 2613, 2298, 2036, 1755, respectively. In this initial condition, the absolute scale of the nozzle is increased tenfold and the vibrational temperature is reduced by 858K, as shown in Fig.5. The freezing point moves down the nozzle throat as the nozzle scale increases. At the centerline vibrational temperature in the different nozzle scales (from 0.5NS to 5NS), the distances x_f from the freezing point to the throat are 451mm, 1241mm, 3091mm, and 9712mm. The freezing point diameters d_f of their corresponding nozzles are 15.7mm, 39.3mm, 92.2mm, and 276.1mm. The ratio d_f/d_t of the freezing point diameter to the throat diameter is 2.86, 3.57, 4.19, and 5.02, respectively. The thermochemical non-equilibrium scale effects are also suitable for the nozzle of FD-21. Fig.7 is a comparison of 0.5NS and NS flow field temperatures. At the centerline vibrational temperature in the 0.5NS and NS nozzles, the distances x_f are 281mm and 875mm. The freezing point diameters d_f of their corresponding nozzles are 98.1mm and 254.1mm, and the ratios d_f/d_t are 9.81 and 12.71, respectively. The absolute scale not only affects the translational temperature and vibrational temperature of the nozzle flow field but also the freezing point. Those phenomena can be explained in the following aspects.

(1) As the nozzle scale increases, the pressure gradient around the throat decreases (see Fig.6). The pressure downstream of the throat increases, which shortens TVERT, as deduced from Eq. (28). Additionally, the decrease of pressure gradient makes the flow velocity decrease and the flow time increase. Both lengthen the transition from equilibrium to freezing, and the flow is close to the equilibrium flow.

(2) Since the nozzles use the same inlet conditions, the velocity u at the nozzle exit is almost identical[25], which is consistent with $h \approx u^2/2$. Because of the freezing of vibrational energy, the increase of the kinetic energy of the airflow in nozzle mainly comes from the translational energy, which leads to the decrease of translational temperature T.

As can be seen from the above conclusion, the flow is frozen not far downstream of the high enthalpy flow throat. Cases 1,3 and 4 in table 1 investigate the thermochemical nonequilibrium scale effects by changing the diameter of the throat alone. Fig.8 shows the distribution of vibrational temperature and translational temperature along the centerline of nozzle. For the throat radius d_t are 20mm, 40mm, and 60mm, the freezing temperatures are 2442K, 2207K, and 2140K, respectively. The distances x_f from the freezing point to the throat are 0.717m, 1.568m, and 3.030m. The freezing point diameters d_f of their corresponding nozzles are 0.254m, 0.536m, and 1.018m. The ratio d_f/d_t of the freezing point diameter to the throat diameter is 12.7, 13.4, and 16.9, respectively. As the throat radius increases, the freezing point moves away from the throat. They can be explained in the following aspects.

(1) The effects of the throat diameter are the same as the scale effects of the nozzle. As the nozzle diameter increases, the pressure gradient around the throat decreases (see Fig.9) and the flow velocity around the throat decrease(See Fig.10) and the flow time increase. Both lengthen the transition from equilibrium to freezing, and the flow is close to the equilibrium flow.

(2) In thermal equilibrium, the increase of the kinetic energy of the gas comes from both molecular translational energy and molecular vibrational energy. Therefore, thermal equilibrium causes the translational temperature and vibrational temperature to decrease. When the vibrational energy freezes, the increase in the kinetic energy of the gas comes only from the translational kinetic energy. The nozzle outlet speed is almost unchanged, which makes the reduction of translational energy deeper and the translational temperature lower.

4.2 Flowfield parameters

Fig.11 shows the Mach number distribution along the centerline. Before the freezing point, the value and evolution of the Mach number are the same. After the freezing point, this phenomenon has changed. It can be explained by the freezing of the vibrational levels. As the nozzle scale increases, the vibrational temperature decreases and the translational temperature increase. With the increase of the nozzle scale, the flow gradually approaches the thermodynamic equilibrium state. As the translational temperature increases, the local sound speed increases (see Table 4a), resulting in the decrease in the Mach number. Fig. 12 can also prove this. The larger the size, the larger the ratio of the exit uniform area radius to the exit radius, which will make the exit Mach number smaller. This is in contradiction with the assumption that the thicker the boundary wall of the nozzle wall and the smaller the Mach number under the same area ratio. It can be known by combining Fig.11 and Fig.12. The influence of thermochemical non-equilibrium scale effects on Mach number is more important than the viscous scale effects.

Cases 1, 3 and 4 in Table 1b are employed to study the effect of the variation throat diameter on the Mach number, as shown in Fig.13. When the throat diameter increases, the flow is close to the equilibrium state. More vibrational energy is transmitted to the translational energy, which makes the translational temperature rise, as deduced from the kinetic energy in Eq. (10). The change in Mach number due to ER and non-equilibrium effects is much more pronounced than the change in Mach number caused by ER alone.

Figs. 14 and 15 show the changes of O_2, O and NO in the axial direction based on the HEG nozzle, respectively. The positions where these components change are the upstream of the freezing point, which is consistent with the changing trend of the vibrational temperature. The flow parameters depend on the dissociation of non-equilibrium before the freezing point. Tables 5a and 5b show the main flowfield parameters in the centerline of the nozzles exit, and the variation trend of the flowfield parameters can be seen. The nozzle flowfield parameters are monotonous to the absolute scale and throat diameter, such as pressure, temperature, sound velocity, Mach number, and species mass fraction. The larger the nozzle scale and throat diameter, the larger the mass fraction of the species N_2 and O_2, but the smaller the mass fraction of the species NO, O, N, NO^+. The species N and NO^+ are trace species, which are not listed here.

As can be seen from Table 5a, when the nozzle scale increases, the degree of the thermal non-equilibrium decreases and the frozen vibrational energy decreases, so that the kinetic energy of the airflow, namely the speed u_∞, increases slightly.

Conclusions

As analyzed in the paper, the high enthalpy nozzle has the thermochemical non-equilibrium scale effects, which has a certain influence on the flow field parameters of the nozzle exit. For a given half cone angle and expansion ratio, the thermochemical non-equilibrium scale effects of the high enthalpy nozzle mainly have the following consequences:

1. As the nozzle scale and expansion ratio increases, the degree of the thermal non-equilibrium decreases, and the frozen vibrational energy decreases, and translational temperature increases. The larger nozzle scale and nozzle expansion ratio can effectively suppress the thermochemical non-equilibrium flow, and is more suitable for simulating the flight environment.
2. The absolute scale affects the freezing point of the high enthalpy nozzle. The larger absolute scale and expansion ratio cause the freezing state of the vibrational dynamics to be delayed. The freezing point moves down the nozzle throat as the nozzle scale and expansion ratio increase.
3. As the nozzle scale increases, the static pressure, and translational temperature at the nozzle exit increase slightly, but the Mach number and vibrational temperature decrease significantly. The larger the nozzle scale and expansion ratio, the larger the mass fraction of the species N_2 and O_2, but the smaller the mass fraction of the species O, N, NO, etc.

Declarations

1. Availability of data and materials

All the data and materials are available in this paper. The data sets supporting the results of this article are included within the article and its additional files.

2. Competing interests

The authors do not have any possible conflicts of interest

3. Funding

The financial support of the National Key Research and Development Plan of China through the project No. 2019YFA0405200 and 2019YFA0405300, National Nature Science Foundation of China

No.11672283, and China Scholarship Council No.201704980060.

4. Authors' contributions

Junmou Shen completed the calculation and analysis of the article, as well as the manuscript of the article. Junmou Shen contributed the most to this article. All authors read and approved the final manuscript.

5. Acknowledgements

The authors gratefully acknowledge the financial support of the National Key Research and Development Plan of China through the project No. 2019YFA0405200 and 2019YFA0405300, National Nature Science Foundation of China No.11672283, and China Scholarship Council No.201704980060.

References

1. Anderson JD. Hypersonic and high temperature gas dynamics. Second edition. AIAA Education Series. 2006.
2. Bushnell DM. Scaling: Wind tunnel to flight. *Rev. Fluid Mech*. 2006; 38: 111-128.
3. Zeng M, Lin ZB, Feng HT. Numerical analysis of non-equilibrium scale effects in hypersonic nozzle. *Propulsion Technology.* 2005; 26(1):38-41. (*Chinese*)
4. Zeitoun D, Boccaccio E, Imbert M. Reactive and viscous flow in hypersonic nozzles. *AIAA Journal* 1994; 32(2): 333-34
5. Hannemann K. High enthalpy flows in the HEG shock tunnel: experiment and numerical rebuilding. *AIAA aerospace science meeting and exhibit*. Reston: AIAA; 2003.
6. Hannemann K, Itoh K, Mee DJ and Hornung HG. Free piston shock tunnels HEG, HIEST, T4 and T5. Experimental Methods of Shock Wave Research, Springer, New York. 2016, p181-264.
7. Zhao W, Jiang ZL, Saito T and Lin JM. Performance of a detonation driven shock tunnel. *Shock Waves* 2005; 14: 53-59.
8. MacLean M, Candler G and Holden M. Numerical evaluation of flow conditions in the LENS reflected shock-tunnel facilities. *AIAA Aerospace Sciences Meeting and Exhibit*. Reston: AIAA; 2005.
9. Shen JM, Ma HD, Li C. Initial measurements of a 2m mach10 free piston shock tunnel at CAAA. *The 31st International Symposium on Shock Waves*; 2017 July 9-14; Nagoya, Japan.
10. Deutsches Zentrum fur Luft - und Raumfahrt (DLR). The high enthalpy shock tunnel Gottingen of the German Aerospace Center(DLR). Journal of Large- Scale Research Facilities. 2018, 4, A133.
11. Miro FM, Beyak ES, Pabio P, et al. High-enthalpy models for boundary-layer stability and transition. *Fluids*. 2019, 31, 044101.
12. Marineau EC, Hornung HG. High-enthalpy nonequilibrium nozzle flow: experiments and computations. *AIAA fluid dynamics conference and exhibit*. Reston: AIAA; 2009.

13. Wang Y, Hu Z, Lu Y. Starting process in a large-scale shock tunnel. *AIAA Journal.* 2016; 54(4): 1240-1249.
14. Chen X, Shen JM, Bi ZX, et al. Review on the development of the free-piston enthalpy impulse wind tunnel and its testing capacities. Journal of Experiments in Fluid Mechanics. 2019, 33(4): 65-80. (*Chinese*)
15. Shen JM, Chen X, Bi ZX, et al. Review on experimental technology of high enthalpy shock tunnel[J]. Acta Aerodynamica Sinica, 2018, 36(4): 543-554. (*Chinese*)
16. Park C. Assessment of two-temperature kinetic model for ionizing air. *Thermophysics* 1989; 3(3): 233-252.
17. Gupta RN, Thompson RA. A review of reaction rates and thermodynamics and transport properties for an 11-species air model for chemical and thermal nonequilibrium calculations to 3000K. NASA; 1990. Report No.: RP-1232.
18. Gnoffo PA, Gupta RN. Conservation equations and physical models for hypersonic air flow in thermal and chemical nonequilibrium. NASA; 1989. Report No.: TP 2867.
19. Grant P, Michael JW. A comparison of methods to compute high temperature gas thermal conductivity. *AIAA thermophyscics conference*. Reston No: AIAA; 2003.
20. Park C. Problems of rate chemistry in the flight regimes of aeroassisted orbital transfer vehicles. *Thermal Design of Aerossisted Orbital transfer Vehicles*. Volume 96 of Progress in Astronautic and Aeronautics. AIAA, 1985; 96: 511-537.
21. Jameson A. Solution of the Euler equations for complex configurations. *AIAA aerospace science meeting*. Reston No: AIAA, 1983.
22. Shima E, Kitamura K. On new simple low-dissipation scheme of AUSM-family for all speeds. *AIAA aerospace science meeting*. Reston No: AIAA; 2009.
23. Spalart PR, Allmaras SR. A one-equation turbulence model for aerodynamic flow. *AIAA aerospace science meeting and exhibit*. Reston No: AIAA; 1992.
24. Li Hanyan. Numerical simulation of hypersonic and high temperature gas flow fields[D]. China Aerodynamics Research and Development Center. 2007.(Chinese)
25. Smirnov NN, Betelin VB, Shagaliev RM, et al. Hydrogen fuel rocket engines simulation using LOGOS code. International Journal of Hydrogen Energy. 2014; 1-9. http://dx.doi.org/10.1016/j.ijhydene.2014.04.150.
26. Smirnov NN, Betelin VB, Shagaliev RM, et al.Accumulation of errors in numerical simulations of chemically reaction gas dynamics. Acta Astronautica. 2015; 117: 338-355. 117http:dx.doi.org/10.1016/j.actaastro.2015.08.013.
27. Frank K. Lu and Dan E. Marren. Advanced Hypersonic Test Facilities. AIAA Education Series. 2002. P21.

Tables

Table 1a Geometrical parameters of the reference nozzles

Case	HCA (°)	d_t (m)	d_e (m)	L (m)	ER
TCM2	10.0	0.006	0.40	1.13	4444
HEG	6.5	0.011	0.88	3.75	6400

Table1b Geometrical parameters based on the FD-21 nozzle

Case	HCA (°)	d_t (m)	d_e (m)	L (m)	ER
1	9.0	0.020	2.00	6.52	10000
2	9.0	0.010	1.00	3.26	10000
3	9.0	0.040	2.00	6.46	2500
4	9.0	0.060	2.00	6.32	1111

Table 2 Initial conditions

Case	P_0 (MPa)	T_0 (K)	C_{N2} (%)	C_{O2} (%)	C_{NO} (%)	C_N (%)	C_O (%)	C_{NO+} (%)
1	101.3	6500	69.08	4.72	14.50	0.68	11.00	0.01
2	48.3	7410	68.72	1.50	9.88	3.20	16.70	0.02

Table 3 Error estimates

Case	TCM2	HEG
Allowable error	5%	5%
Grid resolution	1251×201	1251×201
Physical time simulated(ms)	3.5	5.0
Number of time steps	3500	5000
Accumulated error	1.23×10^{-7}	1.23×10^{-7}
Allowable number of time steps	1.63×10^{11}	1.63×10^{11}
Reliability Rs	4.67×10^{7}	3.27×10^{7}

Table 4a Comparison of flow parameters in the TCM2 nozzle

Results	T (K)	Ma	C_{N2} (%)	C_{O_2} (%)	C_{NO} (%)	C_O (%)	C_N (%)
TCM2	356	11.2	73.23	17.43	7.44	2.04	--
7S2T	358	11.6	73.27	17.82	7.60	1.31	2.6E-7
5S2T	360	11.5	73.17	17.57	7.41	1.93	1.5E-8

Table 4b Comparison of flow parameters in the HEG nozzle

Results	P (Pa)	T (K)	u_∞ (m/s)	C_{N2} (%)	C_{O_2} (%)	C_{NO} (%)	C_O (%)	C_N (%)
HEG	713	694	4776	73.56	13.40	5.09	7.96	1.0E-8
7S2T	701	723	4842	74.01	13.75	4.96	7.25	1.4E-7
5S2T	705	720	4823	73.94	13.48	5.03	7.83	1.8E-8

Table 5a Comparison of flow parameters in the centerline at nozzle outlet in the HEG nozzle

Results	P (Pa)	T (K)	a (m/s)	u_∞ (m/s)	Ma	C_{N2} (%)	Co_2 (%)	C_{NO} (%)	C_O (%)
0.5NS	652	706	527	4804	9.1	74.03	15.34	5.35	5.24
NS	701	723	536	4842	9.0	74.21	16.35	4.96	4.55
2NS	737	801	558	4869	8.7	74.40	17.36	4.55	4.46
5NS	881	917	596	4890	8.2	74.62	18.57	4.02	4.02

Table 5b Comparison of flow parameters in the centerline at nozzle outlet based on the FD-21 nozzle

Results	P (Pa)	T (K)	a (m/s)	u_∞ (m/s)	Ma	C_{N2} (%)	Co_2 (%)	C_{NO} (%)	C_O (%)
0.5NS	63	301	342	4852	13.4	73.66	16.24	6.12	3.94
NS	69	343	367	4903	13.2	74.12	16.00	5.05	4.82
dt=40	453	670	511	4875	9.5	74.31	16.84	4.73	4.10
dt=60	1489	984	619	4832	7.8	74.42	17.43	4.49	3.64

Figures

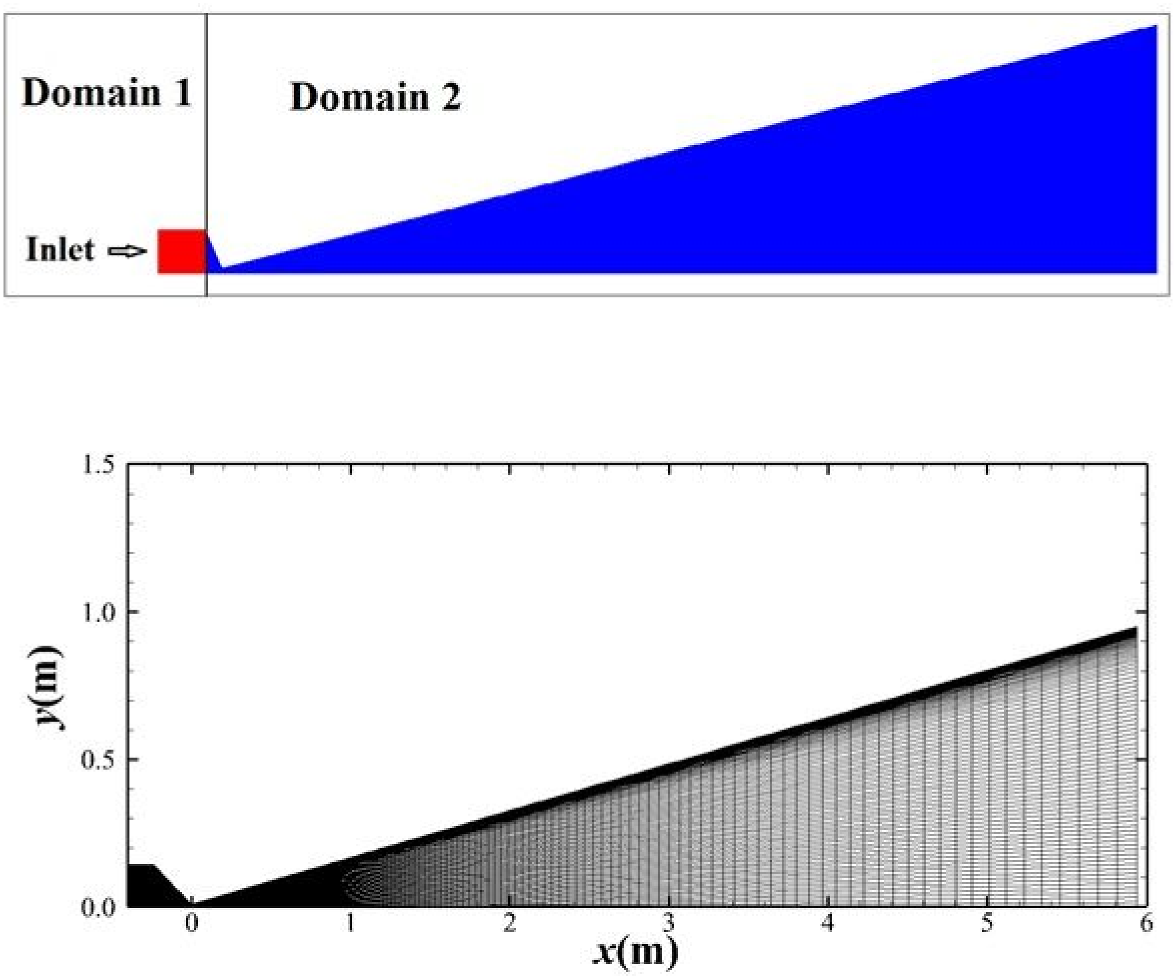

Figure 1

Computational domain. (a) The different domains. (b) Computational grid

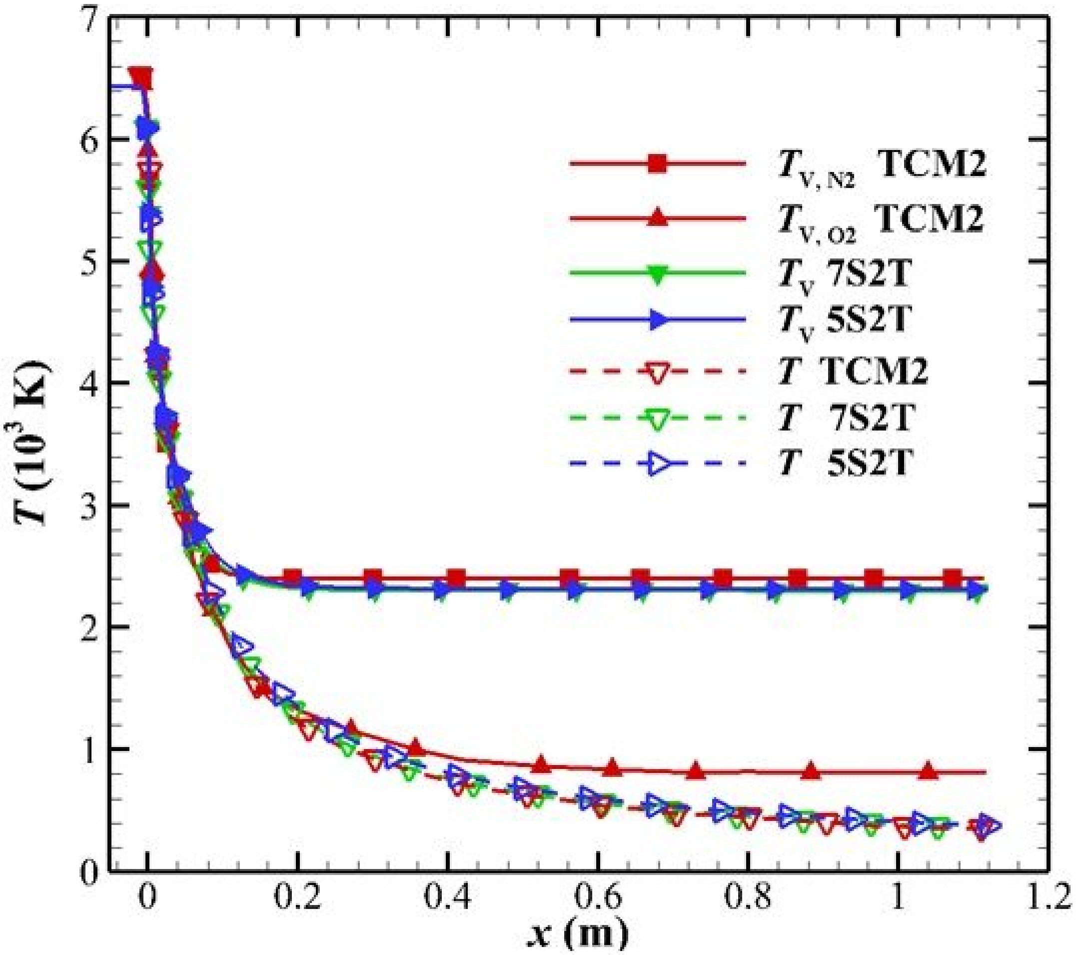

Figure 2

Comparison of the centerline temperature distributions

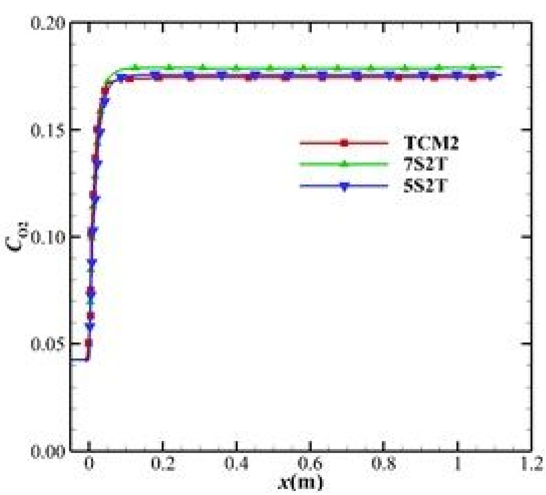

Figure 3

Comparison of the centerline O2 mass fraction distributions

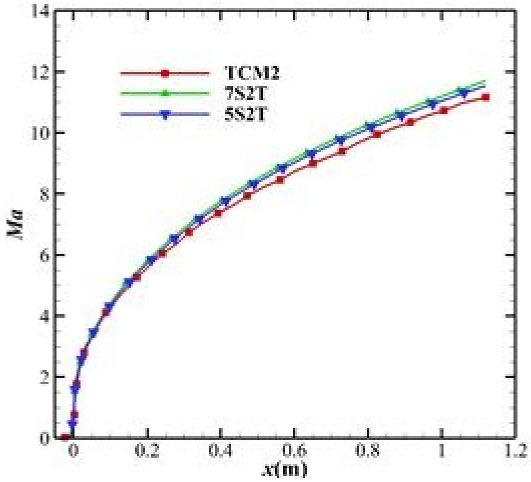

Figure 4

Comparison of the centerline Mach number distributions

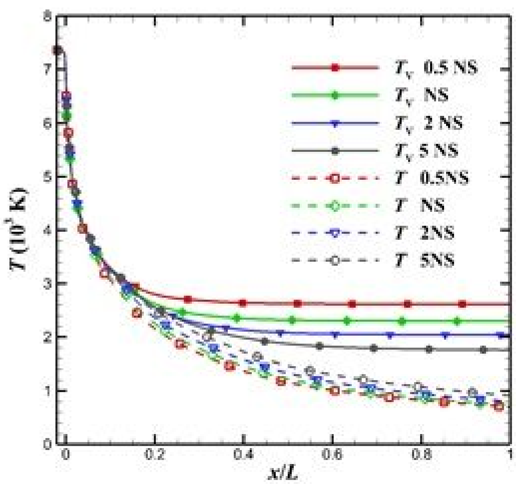

Figure 5

Comparison of the centerline temperature distribution based on the HEG nozzle

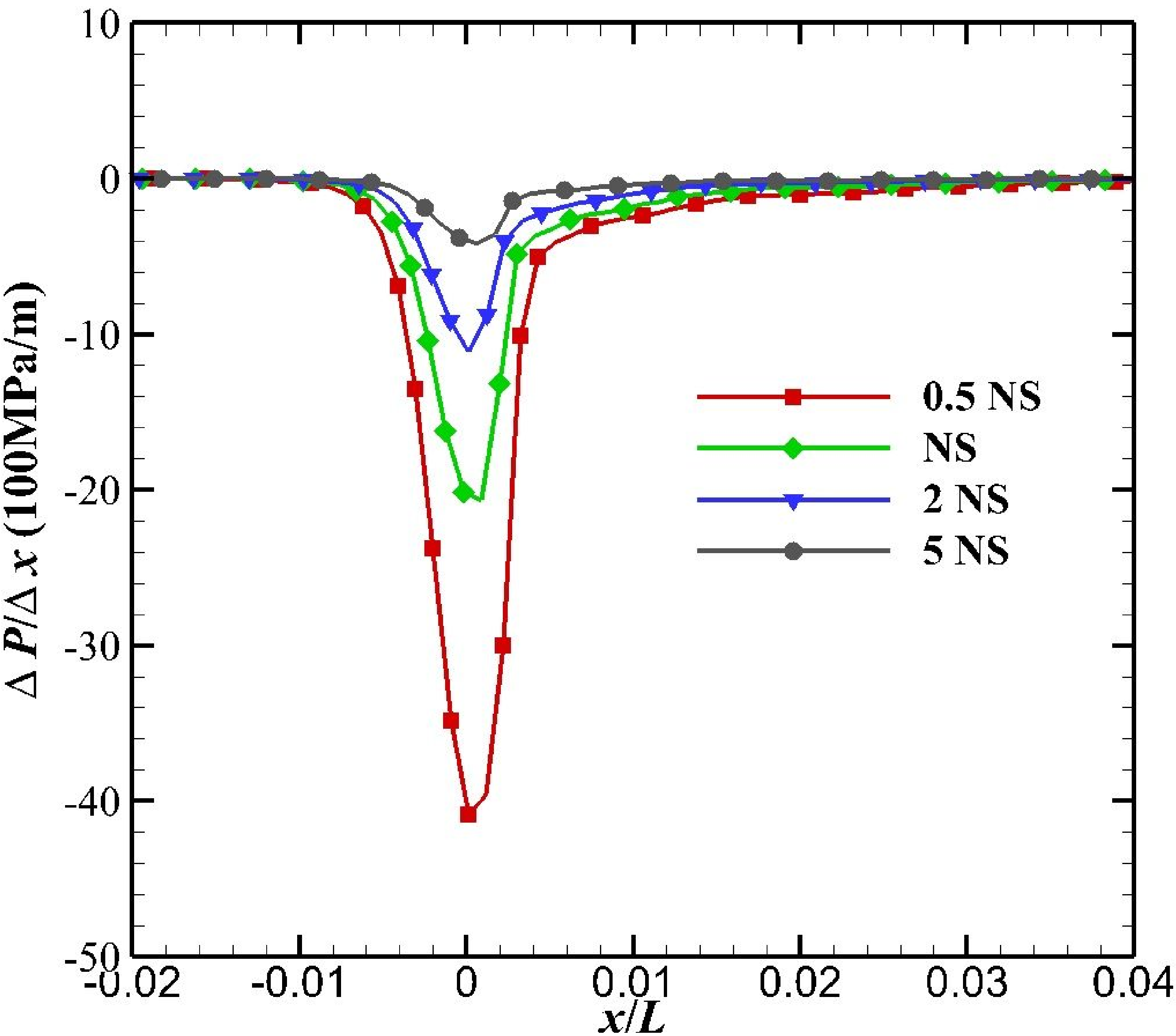

Figure 6

Comparison of the centerline pressure gradient distribution based on the HEG nozzle

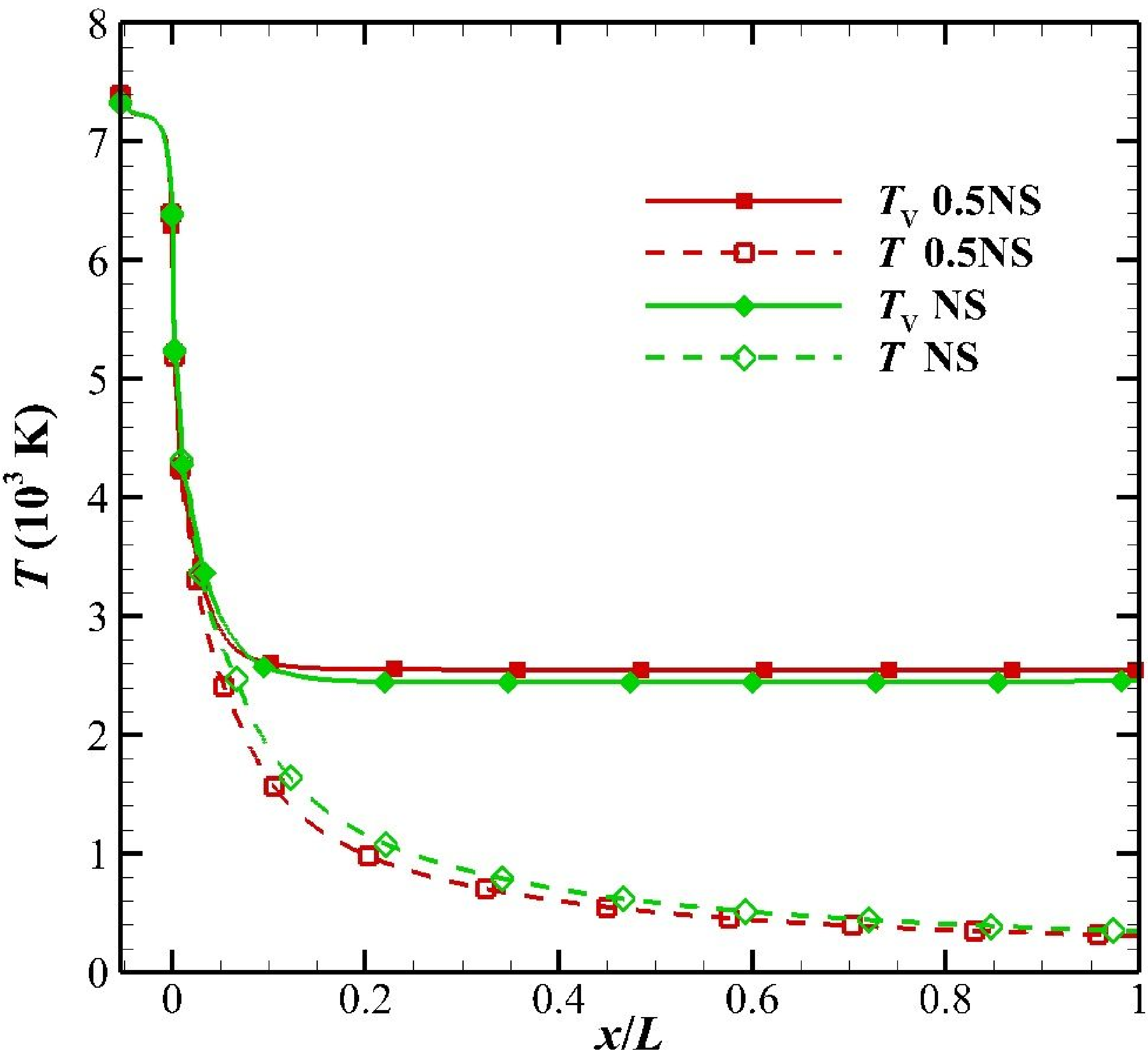

Figure 7

Comparison of the centerline temperature distribution based on the FD-21 nozzle

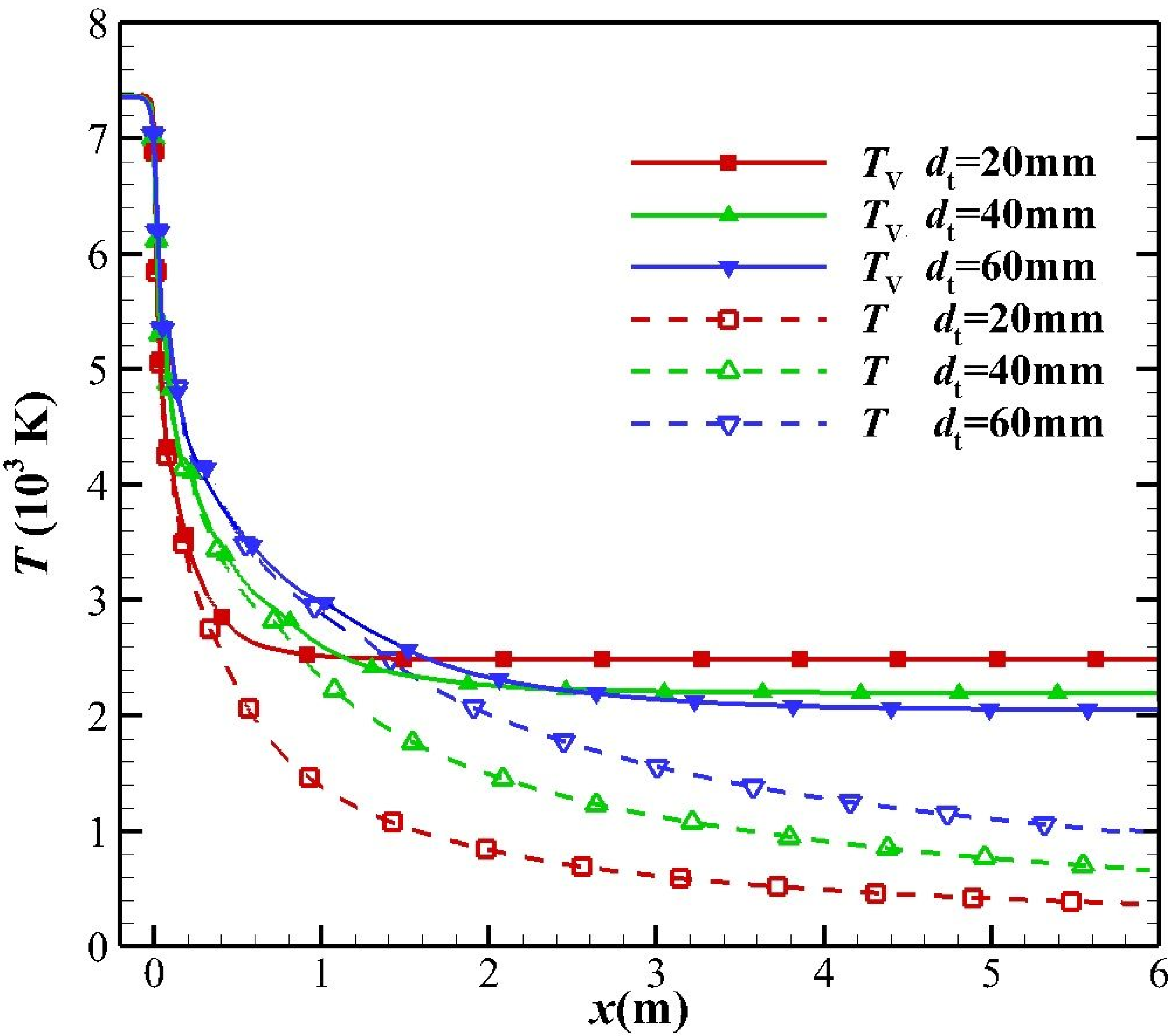

Figure 8

Comparison of centerline temperature distributions based on the different throat diameter

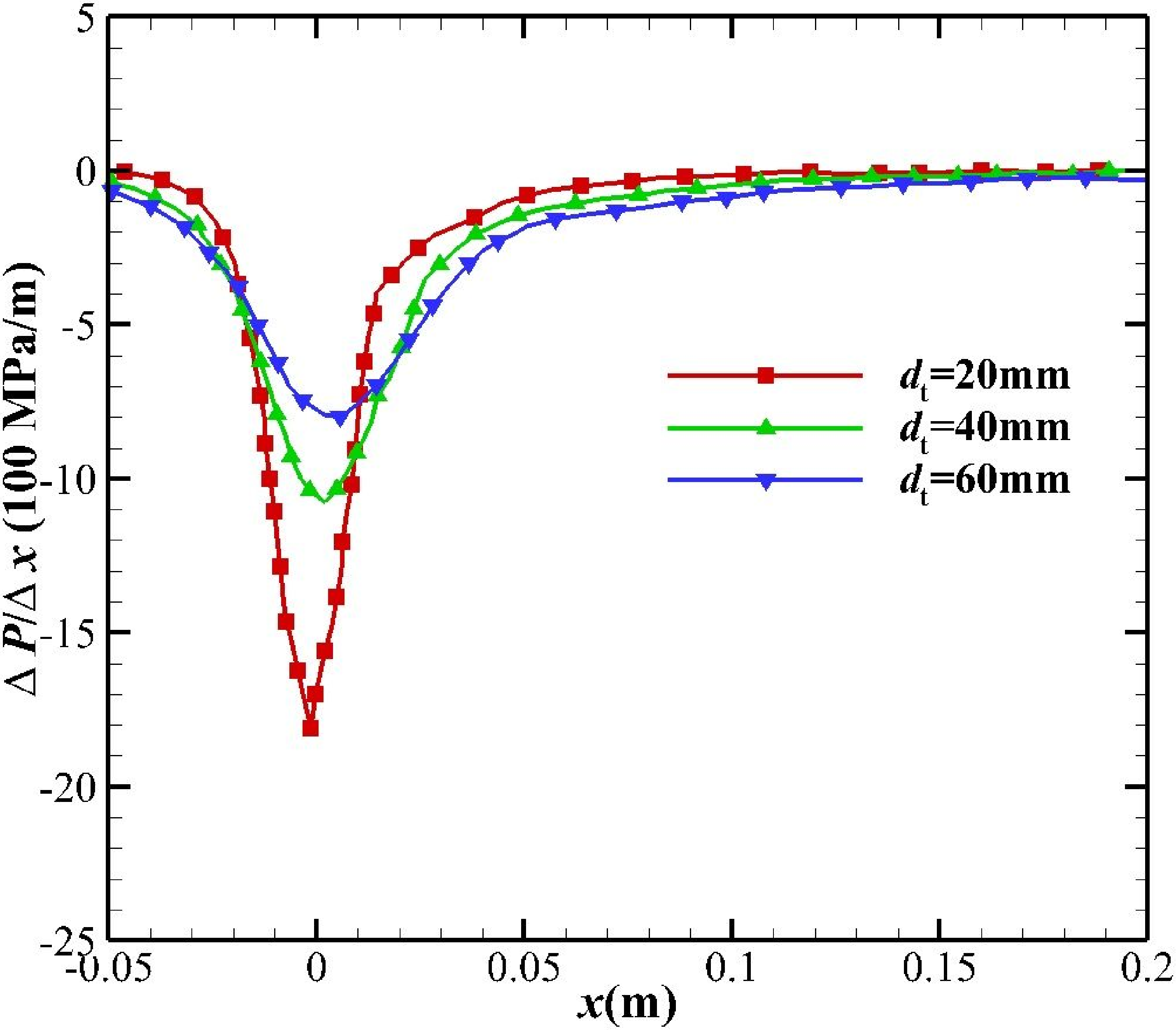

Figure 9

Comparison of centerline pressure gradient distribution based on the different throat diameter

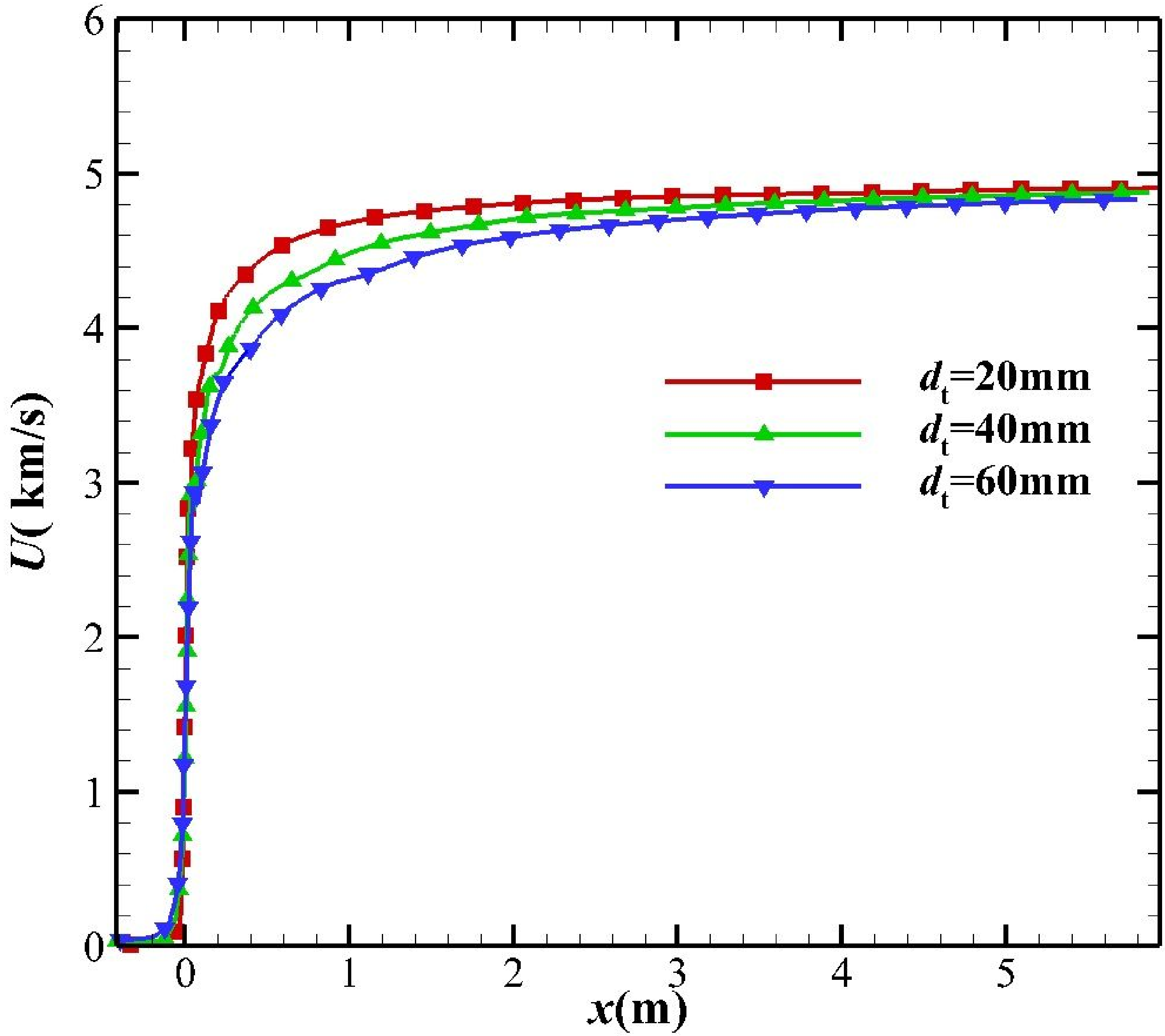

Figure 10

Comparison of centerline velocity distributions based on the different throat diameter

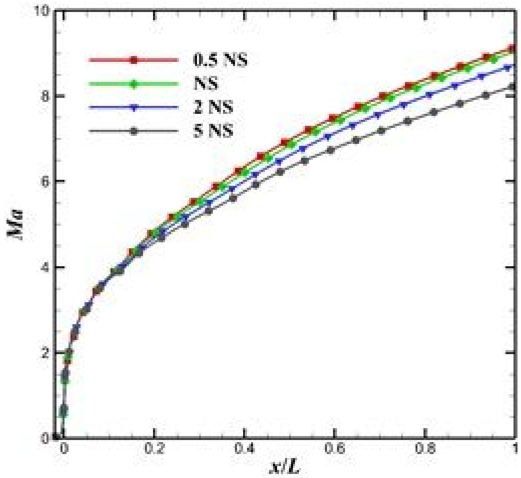

Figure 11

Comparison of the centerline Mach number distribution based on the HEG nozzle

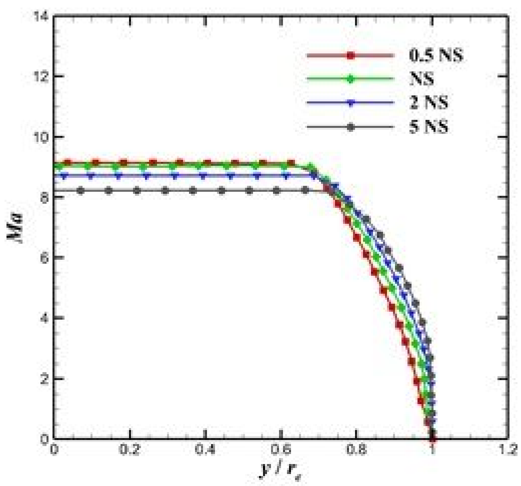

Figure 12

Comparison of the exit Mach number distribution based on the HEG nozzle

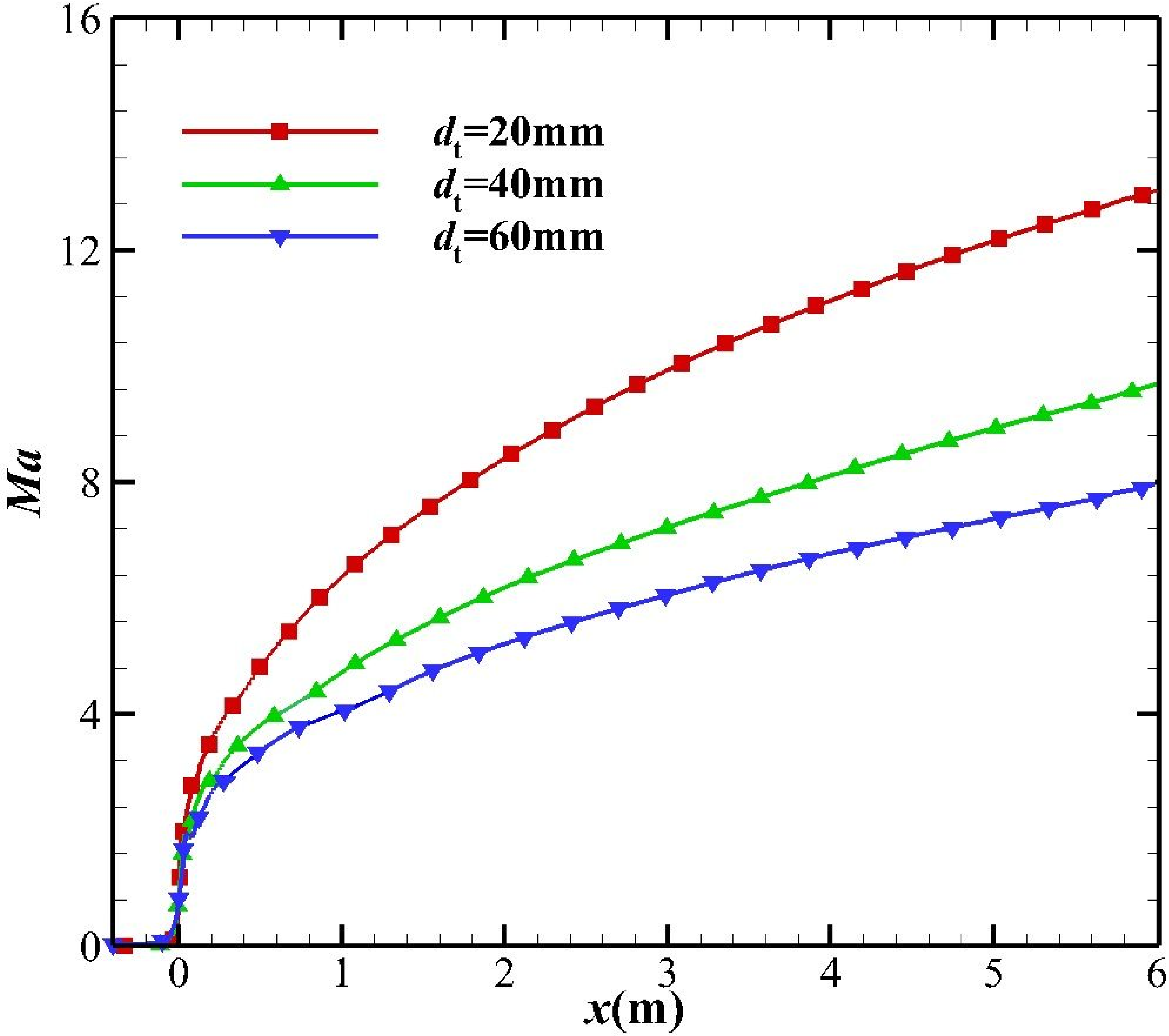

Figure 13

Comparison of the exit Mach number distribution based on the FD-21 nozzle

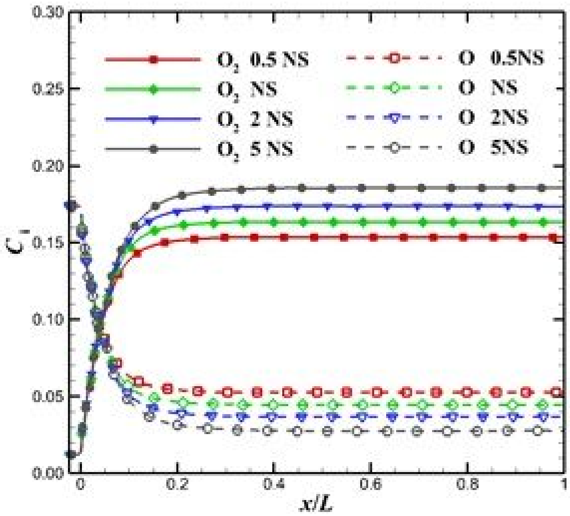

Figure 14

Comparison of the centerline O2 and O mass fraction distribution based on the HEG nozzle

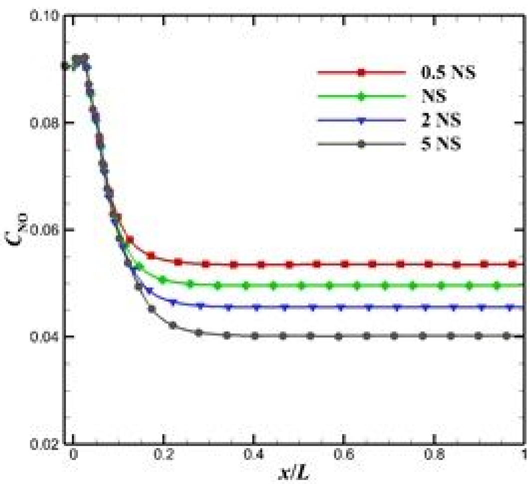

Figure 15

Comparison of the centerline Mach number distribution based on the HEG nozzle

Supplementary Files

This is a list of supplementary files associated with this preprint. Click to download.

- Verificationofcalculationprocedure.docx
- Numericalmethods.docx